Available online at www.sciencedirect.com
ScienceDirect
Journal of Computational Physics 227 (2008) 7543–7560
JOURNAL OF COMPUTATIONAL PHYSICS
www.elsevier.com/locate/jcp

A Lagrangian finite element method for simulation of a suspension under planar extensional flow

M. Ahamadi *, O.G. Harlen

Department of Applied Mathematics, University of Leeds, Leeds LS2 9JT, United Kingdom

Received 14 August 2007; received in revised form 2 January 2008; accepted 23 April 2008
Available online 13 May 2008

Abstract

A numerical simulation of a suspension of two-dimensional solid particles in a Newtonian fluid under planar extensional flow is presented. The method uses a finite element solution of the flow with a unit cell within the self-replicating lattice for planar extensional flow identified by Kraynik and Reinelt [A.M. Kraynik, D.A. Reinelt, Extensional motions of spatially periodic lattices, Int. J. Multiphase Flow 18 (1992) 1045]. This is implemented using a quotient space representation that maps all points space onto points within the unit cell. This mapping is preserved by using fully Lagrangian grid movement, with grid quality preserved by a combination of Delaunay reconnection and grid adaptivity. The no-slip boundary conditions on the particles are enforced weakly via a traction force acting as a Lagrange multiplier. The method allows simulations of suspensions under planar extensional flow to be conducted to large strains in a truly periodic cell. The method is illustrated for both isotropic and anisotropic two-dimensional particles and can be easily extended to viscoelastic fluids and to non-rigid particles.

Keywords: Finite elements (65M60); Fluid mechanics; Suspensions (76T20); Planar extension; Periodic boundary conditions

1. Introduction

Particle suspensions have a wide variety of industrial uses and also characterise many food stuffs and biological fluids. Even in Newtonian fluids, suspensions exhibit complex rheological proprieties such as non-zero normal stress differences in shear. The challenge is to understand how these macroscale proprieties arise from the mesoscale structure on the scale of the suspended particles. Despite a considerable amount of progress in the theory of suspensions over the past century, the question of the detailed interactions between solids and liquids is still open and direct simulations of the exact particle motions in liquid provide an important tool for studying the rheology of such multiphase systems.

For Newtonian fluids a number of different simulation techniques have been developed. These include the Stokesian dynamics method of Brady and Bossis [4], dissipative particle dynamics [3] and the lattice Boltzmann method [6]. Several different finite element based simulation techniques have also been developed.

* Corresponding author.
E-mail address: malidi@maths.leeds.ac.uk (M. Ahamadi).

0021-9991/$ - see front matter © 2008 Elsevier Inc. All rights reserved.
doi:10.1016/j.jcp.2008.04.035

Hu [14] used an Arbitrary Lagrangian method to deal with the time-dependent flow domain of the fluid region in an evolving suspension. An alternative method developed by Glowinski et al. [9] used a Lagrange multiplier fictitious domain method to impose the boundary conditions on the particles. Recently Hwang et al. [13] extended the fictitious domain method to apply sliding biperiodic boundary conditions for a suspension of particles under shear.

In principle the bulk rheology of the suspension is found by subjecting an infinite domain of suspension to an average velocity gradient. This can achieved experimentally provided that the suspended particles are small compared to gap size in the rheometer. In numerical simulations the infinite domain is replaced by a spatially periodic structure based upon a unit cell containing a limited number of particles. The most commonly studied flow is simple shear flow, as this is the easiest flow to reproduce experimentally and it is relatively straightforward to impose the spatially periodic motion of the unit cell on a self-replicating lattice. However, in this paper we shall consider planar extension or pure shear flow. Planar extensional flow occurs when a fluid is extended in one direction and contracted in the perpendicular direction as shown in Fig. 1. The rheological properties of suspensions in extensional flow are important in a number of areas, including the spinning of multiphase synthetic textile fibres. Despite extensional flow being studied extensively both theoretically and experimentally [19], there are relatively few numerical simulations of suspensions in extensional flows [7,12].

Unlike simple shear flow, extensional flow involves a change in the shape of the unit cell within the computational domain. In this study we use the self-replicating Kraynik–Reinelt lattice structure to impose the periodic structure on a two-dimensional computational domain undergoing planar extension. All the particles considered in this paper are hard non-Brownian circular or elliptical particles with aspect ratio less than 10, however, the methodology can easily be extended to other particle shapes. A fully Lagrangian finite element method is used to solve the flow around the particles. For a Newtonian fluid the principal advantage of this approach is that it provides a natural way to implement the biperiodic boundary conditions and particle motions in the Kraynik–Reinelt lattice. However, for a viscoelastic fluid it has further advantage of enabling the constitutive equation to be solved in the co-deforming frame of the fluid [10]. The suspended particles are modelled by imposing a surface force density around the surface of each particle that acts as a Lagrange multiplier to enforce the fluid inside each particle to behave as a rigid solid.

2. Computational domain

The idealised problem we wish to consider is a two-dimensional unbounded domain, $\Omega_\infty(t)$, containing non-Brownian hard circular or ellipsoidal particles suspended in Newtonian fluid under a planar extensional

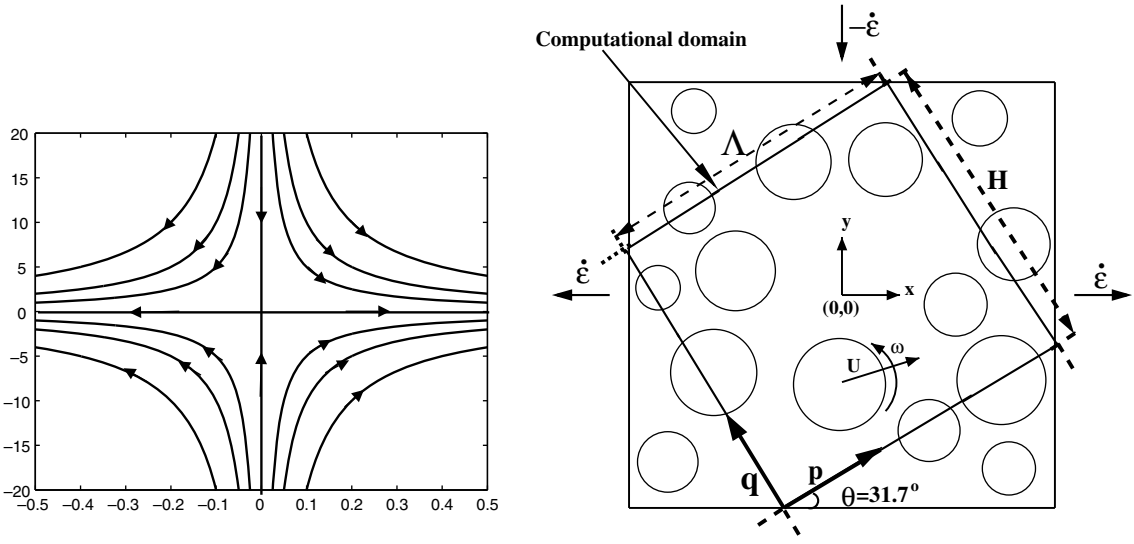

Fig. 1. (a) Particle paths in planar extensional flow. (b) The unit cells in the critical lattice.

flow. In order to make the computations tractable we approximate the fluid microstructures by a spatially periodic fluid microstructure. Therefore we solve the flow in an initially rectangular unit cell of size $H \times \Lambda$ containing N particles, $\Omega(t)$ that when periodically extended covers the infinite domain.

Under the action of the velocity gradient, the unit cell within the lattice deforms and in order to be able to continue to large strains it is desirable to use a self-replicating lattice that recovers its original geometry after a period of strain. In shear flow, this can be achieved using the Lees–Edwards [17] lattice in which cells slide across one another in layers parallel to the flow direction. However, in a purely extensional flow (see Fig. 1b), a rectangular lattice aligned along the principle flow axes will not periodically replicate its structure. A lattice of this type, suggested by Heyes [11] is used in the simulation method developed by Hwang and Hulsen [12] for planar elongational flow of suspensions in a Newtonian fluid. However, because the aspect ratio of the unit cell increases exponentially in time their simulations are limited to moderate strains. D'Avino et al. [7] have recently developed an alternative fixed grid method for simulating extensional flow. This does not use periodic boundary conditions but uses a three layer domain in which particles leaving the domain are reintroduced at random positions on the inlet boundaries in order to achieve steady state.

Kraynik and Reinelt [16] found a family of periodically replicating lattices for planar extensional flow. In particular they showed that the square lattice with the minimum period for replication was one where the sides are aligned at an angle of approximately 31.7° to the principal axes of the flow. Unlike the Heyes structure, this Kraynik–Reinelt structure allows calculations to be performed indefinitely since the shape of the initial unit cell may be recovered after each strain period, ϵ_p. In this paper we show how the Kraynik–Reinelt lattice structure may be implemented in a finite element simulation by using an appropriate image system to map positions in the infinite domain $\Omega_\infty(t)$ to positions in the computational domain, $\Omega(t)$.

2.1. Kraynik–Reinelt lattice

In this section we outline the main result of the Kraynik–Reinelt lattice structure, further details are given in Ref. [16]. As depicted in Fig. 1, we define the x and y direction to be the axes of extension and compression respectively in a flow with strain rate $\dot{\epsilon}$. A two-dimensional square lattice $L(t) = n_1\mathbf{p}(t) + n_2\mathbf{q}(t)$, where $\mathbf{p}(t)$, $\mathbf{q}(t)$ are linearly independent basis vectors and n_1, n_2 integers, is reproducible or *strain periodic* if and only if there exists an integer matrix,

$$N = \begin{bmatrix} N_{11} & N_{12} \\ N_{21} & N_{22} \end{bmatrix}, \tag{1}$$

such that

$$\begin{aligned} \mathbf{p}(t) &= \mathbf{D}(t)\mathbf{p}^0 = N_{11}\mathbf{p}^0 + N_{12}\mathbf{q}^0, \\ \mathbf{q}(t) &= \mathbf{D}(t)\mathbf{q}^0 = N_{21}\mathbf{p}^0 + N_{22}\mathbf{q}^0, \end{aligned} \tag{2}$$

where $\mathbf{D}(t) = \begin{bmatrix} e^{\dot{\epsilon}t} & 0 \\ 0 & e^{-\dot{\epsilon}t} \end{bmatrix}$ is the strain. Here, the vectors $\mathbf{p}^0 = \begin{bmatrix} p_1^0 \\ p_2^0 \end{bmatrix}$ and $\mathbf{q}^0 = \begin{bmatrix} q_1^0 \\ q_2^0 \end{bmatrix}$ are the initial linearly independent lattice basis vectors, which satisfy $\mathbf{p}^0 \cdot \mathbf{q}^0 = 0$ for a square lattice.

The vector equations (2) can be rewritten in the form of the following two eigenvector problems,

$$\begin{bmatrix} N_{11} - \lambda & N_{12} \\ N_{21} & N_{22} - \lambda \end{bmatrix} \begin{bmatrix} p_1^0 \\ q_1^0 \end{bmatrix} = \begin{bmatrix} 0 \\ 0 \end{bmatrix} \quad \text{and} \quad \begin{bmatrix} N_{11} - \lambda^{-1} & N_{12} \\ N_{21} & N_{22} - \lambda^{-1} \end{bmatrix} \begin{bmatrix} p_2^0 \\ q_2^0 \end{bmatrix} = \begin{bmatrix} 0 \\ 0 \end{bmatrix}, \tag{3}$$

where $\lambda = e^{\dot{\epsilon}t}$.

The problem of reproducibility has now been reduced to finding an eigenvalue λ, the strain period, with eigenvectors, $\begin{bmatrix} p_1^0 \\ q_1^0 \end{bmatrix}$ and $\begin{bmatrix} p_2^0 \\ q_2^0 \end{bmatrix}$ giving the basis vectors of the lattice. For a square lattice the basis vectors must be orthonormal and so can be written in the form,

$$\mathbf{p}^0 = \begin{bmatrix} \cos(\theta) \\ \sin(\theta) \end{bmatrix}, \quad \mathbf{q}^0 = \begin{bmatrix} -\sin(\theta) \\ \cos(\theta) \end{bmatrix}, \tag{4}$$

where the angle θ must satisfy

$$\theta = \tan^{-1}\left(\frac{N_{11} - e^{\epsilon_p}}{N_{12}}\right). \tag{5}$$

The integer matrix with the minimum eigenvalue is found to be $N_{11} = 2$, $N_{12} = N_{21} = -1$ and $N_{22} = 1$ for which the Hencky strain period $\epsilon_p = \log \lambda$ is equal to

$$\epsilon_p = \log\left(\frac{3+\sqrt{5}}{2}\right) = 0.9624.$$

The corresponding lattice angle θ is given by

$$\theta = \tan^{-1}\left(\frac{2}{1+\sqrt{5}}\right) = 31.7^\circ.$$

Thus for this initial orientation the square lattice will reproduce itself after a strain of ϵ_p in the sense that vertices of the original lattice move to other vertex points of this lattice. Note that the period of reproducibility depends only on the Hencky strain and so this lattice may be used for a variable strain-rate simulation provided that the principle axes of strain remain constant.

3. Governing equations

Consider a flow described by the mapping $\psi(\boldsymbol{\mathcal{X}}, t)$ relating the position of a fluid particle at time t to its Lagrangian coordinate, $\boldsymbol{\mathcal{X}}$ in the original unit cell, $\Omega(t_0)$,

$$\mathbf{x} = \psi(\boldsymbol{\mathcal{X}}, t). \tag{6}$$

Assuming the flow is incompressible, isothermal and inertialess, the equations of conservation of momentum and mass are given respectively by

$$\begin{cases} \sigma_{ij,j} = 0 & \text{in } \Omega, \\ u_{i,i} = 0 & \text{in } \Omega. \end{cases} \tag{7}$$

Here $u_i = \dot{\psi}_i \circ \psi^{-1}$ are the components of the spatial velocity vector, $\Omega = \psi(\Omega(t_0))$ is the flow domain at time t with boundary $\partial\Omega = \partial\psi(\Omega(t_0))$. For a Newtonian fluid, the Cauchy stress tensor σ_{ij} is given by

$$\sigma_{ij} = 2\mu d_{ij} - p\delta_{ij}, \tag{8}$$

where μ is the fluid viscosity, d_{ij} is the rate of deformation tensor defined as

$$d_{ij} = \frac{1}{2}(u_{i,j} + u_{j,i}) \tag{9}$$

and p is the pressure.

The extensional flow is imposed through the boundary conditions of the computational domain, which will be discussed in Section 5.

3.1. Particles

The filler particles are assumed to be rigid and subject to zero net force and couple. Assuming that there is no slip between the filler particles and the fluid matrix, the fluid velocity at the surface of particle l is given by

$$\mathbf{u} = \mathbf{U}_l + \boldsymbol{\omega}_l \times (\mathbf{x} - \mathbf{X}_l), \quad l = 1, \ldots, N, \tag{10}$$

where $\mathbf{U}_l$ and $\boldsymbol{\omega}_l = \omega_l \hat{\mathbf{z}}$ are the unknown velocity and angular velocity of particle l (with $\hat{\mathbf{z}}$ the unit vector in the $\hat{\mathbf{z}}$ direction). To enforce these boundary conditions we impose a surface force density

$$f_i^l(s) = \sigma_{ij} n_j, \tag{11}$$

around the surface of the particle l as a Lagrange multiplier to force the fluid inside particle l to behave as a rigid solid. Here n_j is the outward unit normal to the boundary of particle P_l.

The angular velocity ω_l and the translational velocity $\mathbf{U}_l$ are found from the conditions of no net force and torque on each particle,

$$\int_{\partial P_l} \mathbf{f}^l \, \mathrm{d}s = 0, \quad l = 1, \ldots, N, \tag{12}$$

$$\int_{\partial P_l} (\mathbf{x} - \mathbf{X}_l) \times \mathbf{f}^l \, \mathrm{d}s = 0, \quad l = 1, \ldots, N, \tag{13}$$

where $\mathbf{f}^l$ is the traction force density vector on particle l. The motions of particles are described by the kinematic equations

$$\frac{\mathrm{d}\mathbf{X}_l}{\mathrm{d}t} = \mathbf{U}_l, \quad \mathbf{X}_l|_{t=0} = \mathbf{X}_{l,0}, \quad l = 1, \ldots, N, \tag{14}$$

$$\frac{\mathrm{d}\Theta_l}{\mathrm{d}t} = \omega_l, \quad \Theta_l|_{t=0} = \Theta_{l,0}, \quad l = 1, \ldots, N, \tag{15}$$

where Θ_l is the angular rotation of particle l. Note that the kinematic equations (14) and (15) are decoupled from Eqs. (10), (12) and (13). Hence these equations of motions can be solved separately by using a standard ordinary differential equation method as we will describe later in Section 6.

The quantity measured in rheological experiments is the spaced averaged stress of the suspension. We shall refer to this as the "bulk" stress to distinguish it from time-averaged quantities. Batchelor [1] derived an expression for the bulk stress in a suspension as sum of the stress in the fluid phase plus a contribution from the surface forces on the particles, in the form

$$\langle \sigma_{ij} \rangle = \frac{1}{V} \left[\int_{V_\mathrm{f}} \sigma_{ij} \, \mathrm{d}V_\mathrm{f} + \frac{1}{2} \int_{\partial P_l} \left[(x_i - X_i) f_j + f_i (x_j - X_j) \, \mathrm{d}s \right] \right], \tag{16}$$

where V_f is the volume of the fluid phase.

4. Finite element formulation

In the Lagrangian finite element method the deforming computational domain is discretized by means of a finite element mesh that deforms with the flow. To render Eqs. (7), (10), (12) and (13) in finite element form, we need to derive their Galerkin weak form. Note that the equation for the fluid momentum (7) is coupled through the no-slip condition equation (10) and through the equations for zero hydrodynamic force and torque satisfied by the traction force. Therefore we shall adopt the combined equation of motion of Glowinski et al. [9] to derive the weak form of the equation for the solid–liquid mixture.

The natural combined velocity space for the fluid and particle velocities is given by

$$\begin{aligned} \mathbb{V} = \{ (\mathbf{v}, \boldsymbol{V}_l, \xi_l) | \mathbf{v} \in H^1(\Omega)^2, \boldsymbol{V}_l \in \mathbb{R}^2, \xi_l \in \mathbb{R}, \quad & \mathbf{v} \\ = \boldsymbol{V}_l + \xi_l \hat{\mathbf{z}} \times (\boldsymbol{x} - \boldsymbol{X}_l) \text{ in } P_l(t), \text{and } \mathbf{v} \text{ biperiodic on } \partial\Omega \}. & \end{aligned} \tag{17}$$

In the distributed Lagrange multiplier method the extended weak form for whole domain can be obtained by removing the constraint equation (10) from the velocity space and enforcing it weakly as a side constraint. This is done by introducing a Lagrange multiplier ($\mathbf{f}^l(s)$ in our case), which can be interpreted as the traction force required to maintain the rigid-body motion of particle $P_l(t)$. In our methodology, the constraint equations (12) and (13) are used to determine the unknown $\mathbf{U}_l$ and $\boldsymbol{\omega}_l$ and therefore they must be incorporated into the final weak form.

$$\int_\Omega -p \nabla \cdot \mathbf{w} \, \mathrm{d}V + \mu \int_\Omega \nabla \mathbf{u} : \nabla \mathbf{w} \, \mathrm{d}V - \sum_{l=1}^{N} \int_{\partial P_l(t)} \mathbf{f}^l \cdot \mathbf{w} \, \mathrm{d}S = 0, \tag{18}$$

$$- \int_\Omega q \nabla \cdot \mathbf{u} \, \mathrm{d}V = 0, \tag{19}$$

$$-\int_{\partial P_l(t)} \boldsymbol{\zeta}_l \cdot (\mathbf{u} - (\mathbf{U}_l + \boldsymbol{\omega}_l \times (\mathbf{x} - \mathbf{X}_l)))\,\mathrm{d}S = 0, \tag{20}$$

$$\int_{\partial P_l(t)} \mathbf{f}^l\,\mathrm{d}S = 0, \tag{21}$$

$$\int_{\partial P_l(t)} \mathbf{f}^l \times (\mathbf{x} - \mathbf{X}_l)\,\mathrm{d}S = 0, \tag{22}$$

where $l = 1, \ldots, N$ and $\mathbf{w}$, q, $\boldsymbol{\zeta}_l$ are respectively the variations for the fluid velocity, pressure, and traction force.

We use triangular $\mathcal{P}_1$–$\mathcal{P}_1$ elements, which have linear continuous pressures and velocities, and a continuous linear interpolation for the force density $\mathbf{f}^l$ around the particles to discretize the weak form (Eqs. (18)–(22)). The element combination $\mathcal{P}_1$–$\mathcal{P}_1$ for the velocity and pressure is unstable to spurious pressure modes. These are removed by introducing a pressure stabilisation in which the weak form of continuity equation (19) is replaced by

$$-\int_\Omega q\nabla\cdot\mathbf{u}\,\mathrm{d}\mathbf{x} - \beta\int_\Omega h^2\nabla q\cdot\nabla p\,\mathrm{d}\mathbf{x} = 0, \tag{23}$$

where h^2 is twice the area of the triangle and β is a positive constant. Following Silvester and Wathen [23], we choose $\beta = 0.025$ as this gives the optimal convergence rate for the Stokes problem.

For a given finite element mesh and particle configuration, the discretization of the weak form Eqs. (18)–(22) leads to the following linear system of algebraic equations

$$\begin{bmatrix} A & B & D & 0 \\ B^T & -C & 0 & 0 \\ D^T & 0 & 0 & E \\ 0 & 0 & E^T & 0 \end{bmatrix} \begin{bmatrix} \widetilde{\mathbf{U}} \\ P \\ \widetilde{\mathbf{F}} \\ \mathbf{V} \end{bmatrix} = \begin{bmatrix} F_1 \\ F_2 \\ F_3 \\ F_4 \end{bmatrix}. \tag{24}$$

The vectors $\widetilde{\mathbf{U}}$, P, $\widetilde{\mathbf{F}}$ and $\mathbf{V}$ are respectively the velocity of the fluid, the pressure, the traction force densities, and a vector composed of the translation and rotational velocities of each particle. The vectors on the right hand side F_i, $i = 1, \ldots, 4$ are forcing term resulting from the Kraynik–Reinelt boundary condition which will be described in the next section. The matrices A, B and $-C$ arise from stabilised Stokes problem for the fluid phase, while the matrices D and E arise from the traction forces and no-slip boundary condition on the particle surface. The linear system of algebraic equations (24) is solved using a preconditioned conjugate residuals method with a block preconditioner of the form suggested by Silvester and Wathen [23].

5. Moving mesh implementation of Kraynik–Reinelt cell

In Section 2.1 we defined the structure of the Kraynik–Reinelt lattice, which provides a periodically replicating lattice for planar extensional flow. The biperiodic boundary conditions also allow particles to migrate through the cell and re-enter through the opposite boundary. In order to satisfy biperiodicity of the discrete finite element initially we generate a biperiodic mesh for the computational domain, $\Omega(t_0)$, in which the nodes on opposite edges are identified as being equivalent points. This equivalence can be extended further by noting that every point in the computational domain has an equivalence class of image nodes in the infinite domain, Ω_∞.

We will use this equivalence class to maintain the periodic structure as the domain deforms. Let $\sim$ be an equivalence relation on $\mathcal{V} = \mathbb{R}^2$ defined by

$$\mathbf{x} \sim \mathbf{r} \Longleftrightarrow \exists m \in \mathbb{Z}, n \in \mathbb{Z} \text{ such that } \mathbf{x} = \mathbf{r} + m\mathbf{p}(t)\Lambda + n\mathbf{q}(t)H \tag{25}$$

and $\mathcal{W} = \{(a,b) \in \mathbb{R}\times\mathbb{R} \text{ such that } 0 \leqslant a \leqslant \Lambda \text{ and } 0 \leqslant b \leqslant H\}$ is the computational domain, $\Omega(t)$. The quotient space $\mathbb{R}^2/\mathcal{W}$ contains all equivalence classes of the equivalence relation (25). Furthermore the function $\mathcal{Q}$ defined as

$$\begin{aligned} &\mathcal{Q} : \mathbb{R}^2 \to \mathbb{R}^2/\mathcal{W}, \\ &\mathbf{x}^{\mathbf{imag}} \mapsto \mathcal{Q}(\mathbf{x}^{\mathbf{imag}}) = [\mathbf{x}^{\mathbf{lattice}}] \end{aligned} \tag{26}$$

is the quotient map allowing us to identify all images. From the general form of the quotient map, Eq. (26), one can derive an explicit relation between a point in $\Omega(t)$ and its images in Ω_∞ and between the velocities and other quantities held at these points.

For planar extensional flow, it follows from Eqs. (2) and (4) that

$$\begin{aligned} x^{\text{imag}} &= x^{\text{lattice}} + m e^{\dot{\epsilon} t} \cos(\theta) \Lambda - n e^{\dot{\epsilon} t} \sin(\theta) H, \\ y^{\text{imag}} &= y^{\text{lattice}} + m e^{-\dot{\epsilon} t} \sin(\theta) \Lambda + n e^{-\dot{\epsilon} t} \cos(\theta) H, \end{aligned} \tag{27}$$

where θ is the orientation angle for the original lattice and $\dot{\epsilon} t$ the Hencky strain. Here the integer pair (m, n) denote the shift in the periodic image. The unit cell corresponds to the points $m = 0$, $n = 0$. However, in order to close the boundary it is necessary to also include points on the top and righthand edges, that are respectively the $n = 1$ and $m = 1$ images of the points on the bottom and lefthand edges. Thus each finite element node in $\Omega(t)$ has an infinite set of image elements that lie outside $\Omega(t)$ with nodes given by images of the node points of the original elements. Consequently in assembling the finite element matrices it is sufficient to ensure that the contribution from each element is included once and once only, but it is does not matter which particular image of the element is used. However, since each node has an infinite set of images it is necessary to define the displacements between nodes on an element uniquely.

We shall define $\mathbf{dx}^{\mathbf{lattice}} = (\mathrm{d}x^{\text{lattice}}, \mathrm{d}y^{\text{lattice}})$ as the displacement between two neighbouring nodes in the mesh, whose $m = 0$, $n = 0$ positions are displaced by $\mathbf{dx}$. Since each point has an infinite set of images displaced by integer multiples of $\Lambda \mathbf{p}(t)$ and $H\mathbf{q}(t)$, we can define $\mathbf{dx}^{\mathbf{lattice}}$ uniquely as the displacement between images that lies in the space

$$\mathbf{dx}^{\mathbf{lattice}} = \mathrm{d}p\mathbf{p}(t) + \mathrm{d}q\mathbf{q}(t) \quad \text{with} \quad -\frac{\Lambda}{2} < \mathrm{d}p \leqslant \frac{\Lambda}{2}, \quad -\frac{H}{2} < \mathrm{d}q \leqslant \frac{H}{2}. \tag{28}$$

In practice, for a reasonably fine mesh, the values of $\mathrm{d}p$ and $\mathrm{d}q$ will be well within these bounds. Using this restriction on $\mathrm{d}p$ and $\mathrm{d}q$ we can find unique values of m and n such that

$$\mathbf{dx} = \mathbf{dx}^{\mathbf{lattice}} + m\mathbf{p}(t)\Lambda + n\mathbf{q}(t)H.$$

The external extensional flow is imposed by the condition that the fluid velocity $\mathbf{u}^{\text{imag}}$ of the (m, n) image is given by the time derivative of the quotient map given in Eq. (26). Consequently the fluid velocity, $\mathbf{u}^{\text{imag}}$ is given by

$$\mathbf{u}^{\text{imag}} = \mathbf{u}^{\text{lattice}} + \dot{\epsilon}(T_u, T_v), \tag{29}$$

where $T_u = m e^{\dot{\epsilon} t} \cos(\theta) \Lambda - n e^{\dot{\epsilon} t} \sin(\theta) H$ and $T_v = -m e^{-\dot{\epsilon} t} \sin(\theta) \Lambda - n e^{-\dot{\epsilon} t} \cos(\theta) H$. The velocity space $\mathcal{V}$ is given by

$$\mathcal{V} = \{\mathbf{v}_h \in (C^0(\Omega))^2 \text{ such that } \mathbf{v}_h|_T \in \mathcal{P}_1 \times \mathcal{P}_1 \text{ for all } T \in \mathcal{T}_h, \quad \mathbf{v}_h \text{ biperiodic on } \partial\Omega\} \tag{30}$$

where $\mathcal{T}_h$ is the regular finite element triangulation of Ω for $\mathbf{u}$ and $\mathcal{P}_1$ is the space of polynomials in two variables of degree one. All other variables, including pressure and those governing fluid microstructure for a viscoelastic fluid, have the same value at each image point.

6. Mesh movement and reconnection

By moving each node with its velocity the connectivity of the grid is preserved. However, a major drawback of using a Lagrangian mesh is that severe deformation-induced mesh distortions develop due to velocity gradients within the fluid, which will degrade the accuracy of the finite element solution. A partial solution to this problem is to retain the nodes as material points, but reconnect them in the way that produces a Delaunay triangulation [8], the dual of the Voronoi tessellation. The Delaunay triangulation ensures global equiangular triangulation in the sense that it maximises the minimum angle in any triangle [22].

The Lagrangian mesh movement combined with Delaunay reconnection and the use of the equivalence class to relate points with their images automatically reproduces the self replicating lattice of Reinelt and Kraynik. This is illustrated in Fig. 2 where the evolution of a very simple mesh consisting of eight triangular elements connecting four replicated points and their appropriate images under planar extension is shown. The initial mesh is shown in Fig. 2a with the square unit cell (indicated by the bold lines) oriented at an angle $\theta = 31.7°$ to the x-axis. Figs. 2b and c show the lattice after a strain of $\frac{1}{2}\epsilon_p$. The original unit cell (shown with solid bold lines in Fig. 2b) is deformed into a parallelogram, however, we can reform an equivalent square unit cell (shown with dashed lines), by replacing $\mathbf{p}$ with $\mathbf{p} + \mathbf{q}$. Between Figs. 2b and c we have performed a Delaunay reconnection. Although we have recovered a square lattice it is not the original lattice as now oriented at 58.3° to the x-axis. Fig. 2d shows the lattice after a strain of $\epsilon_p = 0.962424$. We can now recover the original square unit cell by choosing appropriate images. A further Delaunay reconnection will reproduce the original grid shown in Fig. 2d.

For the simulations containing particles we first generate a non-periodic grid by assigning the nodes on the boundaries of the particles and the unit cell, but being careful to ensure that the cell boundaries are matched to satisfy periodicity particularly when a particle crosses a boundary. We then use the "Triangle" grid generation program [21] to generate an initial grid in the unit cell. Finally the boundary points are relabelled so that equivalent points have the same label forming a periodic grid. The region inside the particles is meshed, but since this region is constrained to perform a solid body rotation it does not need to be included in the assembly. The only modification to mesh movement and reconnection is that the Delaunay reconnection is

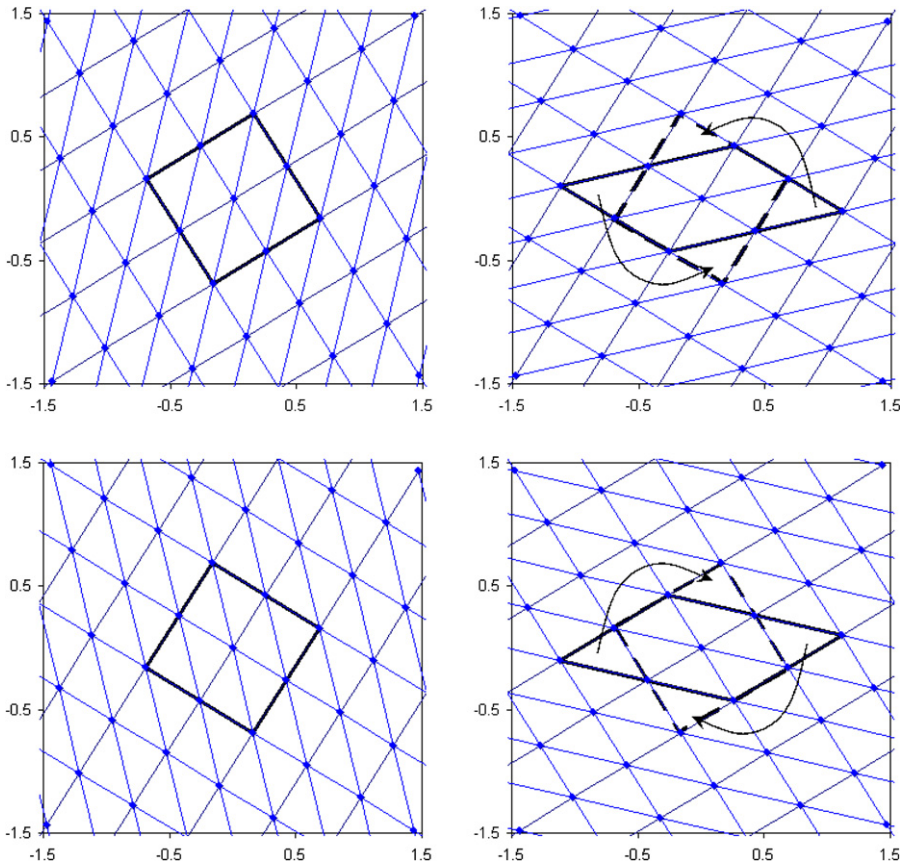

Fig. 2. A simple example showing how the mesh movement and reconnection replicate the unit cell after a strain of $\epsilon_p = 0.9624$. (a) The initial lattice with a unit cell made up of eight triangular elements. (b) The lattice after a strain of $\frac{1}{2}\epsilon_p$. The initial unit cell is shown with the solid line, while the dashed line shows an equivalent square unit cell formed by replacing two of the elements with their images. (c) The lattice after a strain of $\frac{1}{2}\epsilon_p$ following a Delaunay reconnection. (d) The lattice after a strain of $\epsilon_p = 0.9624$. The original unit cell and lattice can be recovered by a further replacement of two elements with their images and a further Delaunay reconnection.

not allowed to reconnect an edge on a particle boundary. However edges on the boundary of the unit cell are reconnected so that the outline of the original cell is lost. As noted earlier, due to the equivalence class it does not matter which image of a triangle is used in the assembly as long as it included once and once only.

Once particles are introduced reconnection alone is not sufficient to maintain mesh quality and so we employ the following methods of grid improvement during the calculation.

(1) At each time step the existing nodes are reconnected where necessary to form a Delaunay triangulation, using an iterative algorithm.
(2) Edges shorter than a minimum length are removed by removing one of the nodes. This minimum length depends upon the distance from the nearest particle boundary.
(3) Triangles with areas greater than a maximum area criterion that depends upon the distance from the nearest particle boundary are split by introducing a new node at the centroid.
(4) After any addition or deletion of nodes the Delaunay triangulation is restored by running the iterative algorithm again.
(5) When particles come close together the minimum length, and maximum area, measures in the region between the particles are reduced to increase the resolution in this region.

The simulation algorithm is as follows:

(1) *Initialization*
- Generate an initial biperiodic mesh with the particles randomly positioned in the fluid (i.e $X_i(t_0)$, $i = 1, \ldots, N$) but not overlapping.
- Find $\widetilde{\mathbf{U}}^{\mathbf{0}}, P^0, \widetilde{\mathbf{F}}^{\mathbf{0}}$ and $\mathbf{V}^{\mathbf{0}}$ by solving Eq. (24).

(2) *Main loop*Given Δt and $t_{\max}$, while $t < t_{\max}$, do
- $t_n = t_{n-1} + \Delta t$.
- Update mesh nodes.
- Update the computational domain configuration by using Eq. (2).
- Update the orientation and position of each particle using a first order finite difference approximation of the kinematic equations (14) and (15).

$$\mathbf{X}(t_n) = \mathbf{X}(t_{n-1}) + \Delta t \mathbf{U}(t_n),$$
$$\mathbf{\Theta}(t_n) = \mathbf{\Theta}(t_{n-1}) + \Delta t \boldsymbol{\omega}(t_n).$$

- Apply the remeshing procedure.
- Find $\widetilde{\mathbf{U}}^{\mathbf{n}}, P^n, \widetilde{\mathbf{F}}^{\mathbf{n}}$ and $\mathbf{V}^n$ by solving Eq. (24).

7. Extensional viscosity and particle orientation

The main material function of interest is the bulk extensional viscosity defined as

$$\langle \eta \rangle = \left\langle \frac{\sigma_{xx} - \sigma_{yy}}{\dot{\epsilon}} \right\rangle.$$

For a Newtonian fluid the planar extensional viscosity is equal to $\eta = 4\mu$ (compared to 3μ for uniaxial extension). For a filled system the extensional viscosity depends upon both the spatial and (for non-circular particles) orientation distributions of the particles, which evolve with increasing strain. In the limit of dilute suspension where the particles are sufficiently far apart there exist analytic results with which we can compare our simulations. We shall also consider the effects of increasing concentration on non-dilute suspensions.

7.1. Circular particles

We begin by considering a single circular particle whose area is a fraction $\Phi = 0.1963$ of the unit cell as shown in Fig. 3. To establish spatial convergence we use four different uniform meshes as described in Table

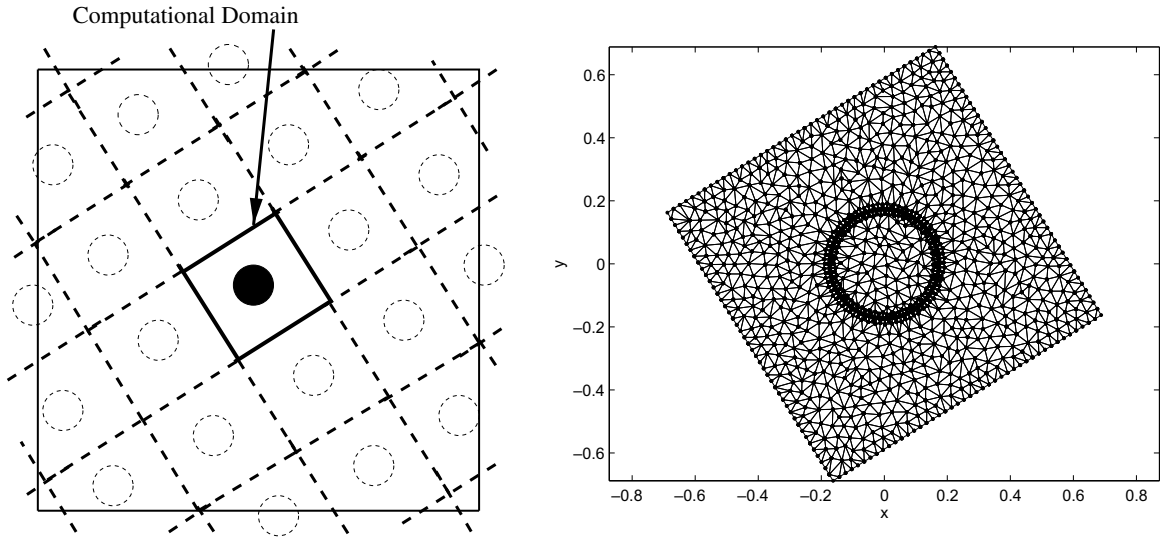

Fig. 3. The computational domain for the single particle problem. (a) The unit cell at time $t = 0$ in relation to its periodic images. (b) The finite element mesh1 used in the calculations described in Table 1.

1. Here, N_b are the number of nodes along each edge of the unit cell, N_p the number of nodes around the particle, and Area min is the threshold value for the area of each triangle that is required by "Triangle". Mesh1 is shown in Fig. 3b. Table 1 shows the computed values of the extensional viscosity at $t = 0$ for these different meshes. This is also shown graphically in Fig. 4 where we plot the extensional viscosity against the inverse of the number of elements, N_e. The results of these four meshes lie approximately on a straight line, indicating that the error in extensional viscosity is proportional to N_e^{-1}, so that the spatial convergence for the extensional viscosity is of order h^2. The reason the convergence is order h^2 and not order h is that the extensional viscosity is proportional to dissipation, which is minimised in the variational statement of the finite element method. In subsequent calculations we have used grids equivalent to mesh3.

The subsequent evolution of the extensional viscosity with strain is shown in Fig. 5a for $\Phi = 0.2827, 0.3318, 0.3848$. The viscosity of the suspension oscillates with a period equal to half that of the self-replicating lattice, due to the hydrodynamic interactions of the particle with its images. The maximum extensional viscosity occurs when the particles are arranged in a square lattice, which occurs twice in each period ϵ_p since the lattice configuration after a strain of $\frac{1}{2}\epsilon_p$ is square, but is rotated relative to its initial configuration. Since the extensional viscosity is periodic, we can define the average extensional viscosity as the time average over a lattice period. This is shown in Fig. 5b as a function of area fraction Φ. Note this periodicity only exists when we have a single circular particle in the unit cell.

In a dilute suspension, the hydrodynamic interactions between the suspended particles are assumed to be negligible, so that results may be obtained by considering a single isolated particle. For a dilute suspension of circular particles there is a two-dimensional analogue obtained by Brady [5] of the Einstein viscosity, given by $\mu_{\text{eff}} = \mu(1 + 2\Phi)$. Therefore the planar extensional viscosity η should tend to $4\mu(1 + 2\Phi)$ in the limit $\Phi \to 0$. This is shown as the dashed line in Fig. 5b. It can be seen that the limiting behaviour at low area fraction does

Table 1
Details of the four finite element meshes used to calculate the extensional viscosity at $t = 0$ for a circular particle of area fraction $\Phi = 0.1963$

Mesh	N_b	N_p	Area min	Elements, N_e	Extensional viscosity, η
Mesh1	32	140	0.0025	1262	5.75953447
Mesh2	44	196	0.001	2296	5.75678527
Mesh3	62	277	5×10^{-4}	4198	5.75501656
Mesh4	88	392	2.5×10^{-4}	7680	5.75408069

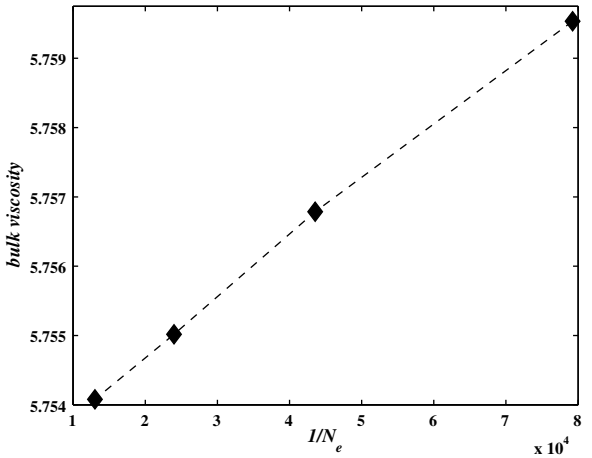

Fig. 4. Plot of the extensional bulk viscosity from Table 1 against $1/N_e$ (proportional to h^2) indicating that the spatial convergence of the extensional viscosity is second order.

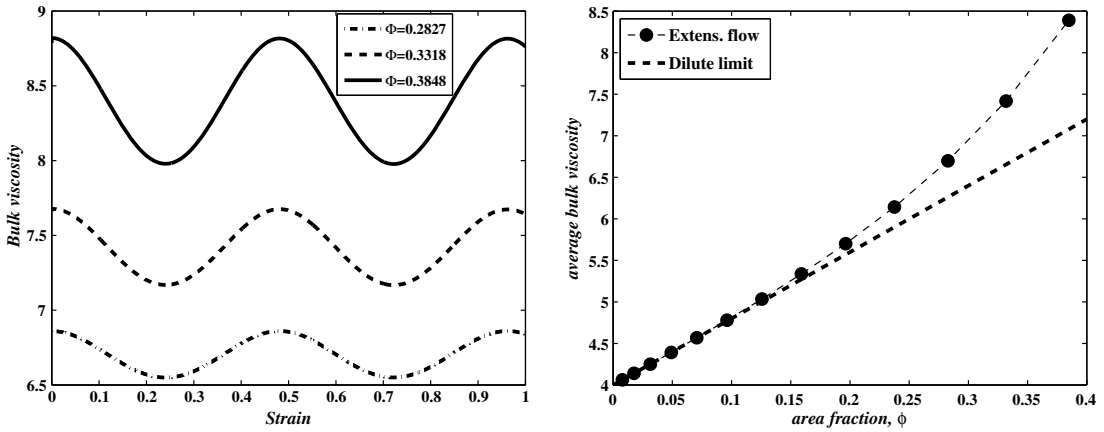

Fig. 5. (a) Extensional bulk viscosity as a function of time for $\Phi = 0.2827, 0.3318, 0.3848$. (b) Time averaged extensional bulk viscosity as a function of area fraction. The dashed line shows the asymptote in the dilute limit, $4\mu(1 + 2\Phi)$.

indeed agree with this asymptotic behaviour, but that hydrodynamic interactions produce a greater enhancement of the viscosity with increasing area fraction. This nonlinear increase will depend upon particle distribution, which is set by the Kraynik–Reinelt lattice. Consequently the results will depend upon the lattice structure chosen. The lattice also imposes a maximum area fraction, equal to $\pi\sqrt{5}/10 = 0.702$ for the particles to not come into contact. The critical lattice used here has the largest maximum area fraction of all the square and hexagonal replicating lattices investigated by Kraynik and Reinelt [16].

In order to remove the symmetry imposed by the lattice system we simulate the motion of multiple particles per box, whose initial positions are chosen at random (subject to them not overlapping). The extensional viscosity is no longer periodic but we can average over a long simulation to obtain average values. In Fig. 6a we compare the average viscosity for 25 circular particles per cell with those obtained with a single particle at equivalent area fractions. Both approach the low volume fraction asymptote as $\phi \to 0$, however, at larger area fraction the 25 particle simulations show a significantly higher average extensional viscosity. This demonstrates that hydrodynamic interactions between close groups of particles provide a disproportionate contribution to the bulk viscosity. This can be seen in Fig. 7 where we show a snapshot of the distribution of the dimensionless principal stress difference, $\Delta\sigma$,

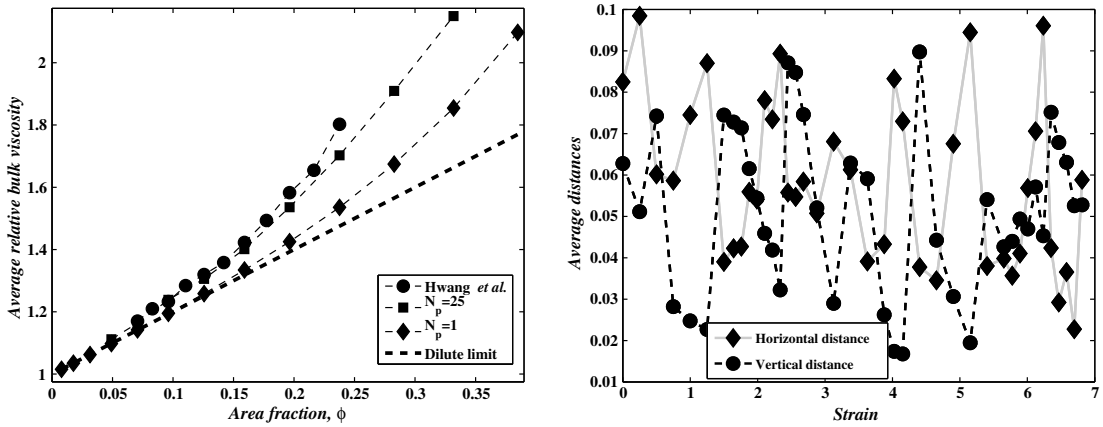

Fig. 6. (a) Average bulk viscosity as a function of area fraction. The full circles are the results of Hwang et al. The square symbols denote simulation with 25 particles per cell at area fractions $\phi = [0.0020, 0.0028, 0.0038, 0.0050, 0.0064, 0.0079, 0.0095, 0.0113, 0.0133]$, and the diamonds show results with a single particle per cell The dashed line shows the dilute asymptote, $4\mu(1 + 2\Phi)$. (b) Plot of the mean horizontal and vertical distances between particles as function of strain.

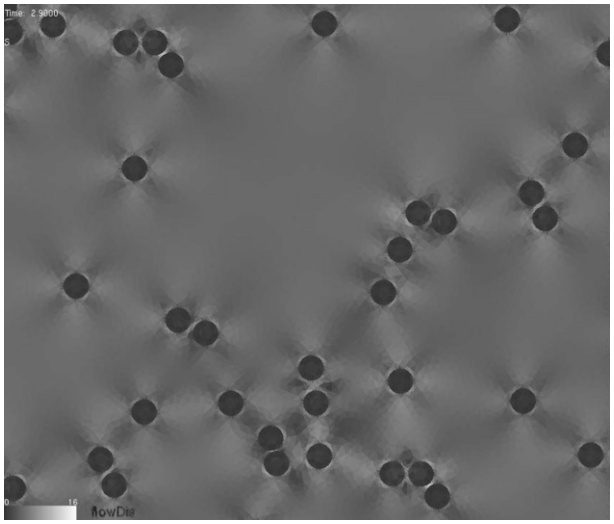

Fig. 7. Snapshot showing the distribution of the dimensionless principal stress difference $\Delta\sigma$ after a strain of 2.9. The scale runs from 0 (black) to 16 (white).

$$\Delta\sigma = \frac{1}{\mu\dot{\epsilon}}\sqrt{(\sigma_{xx} - \sigma_{yy})^2 + 4\sigma_{xy}^2}.$$

Except in regions close to the suspended particles $\Delta\sigma$ is approximately equal to 4, its value in the absence of particles. However, at this particular snapshot the maximum value of $\Delta\sigma$ is more than four times this value and is found in the gaps between close particles (see Fig. 8).

The bulk viscosities obtained from the 25 particle simulations are found to be in good agreement with those obtained by Hwang and Hulsen [12] and D'Avino et al. [7] that use different methods for imposing the boundary conditions on extensional flow. The results obtained by Hwang et al. are shown in Fig. 6a. Although the bulk viscosity values are in approximate agreement, we find qualitatively different results for the particle distributions. Both Hwang and Hulsen [12] and D'Avino et al. [7] find that the average distance in the direction of the horizontal (extensional) axis between nearest neighbours becomes slightly larger than the distance in the

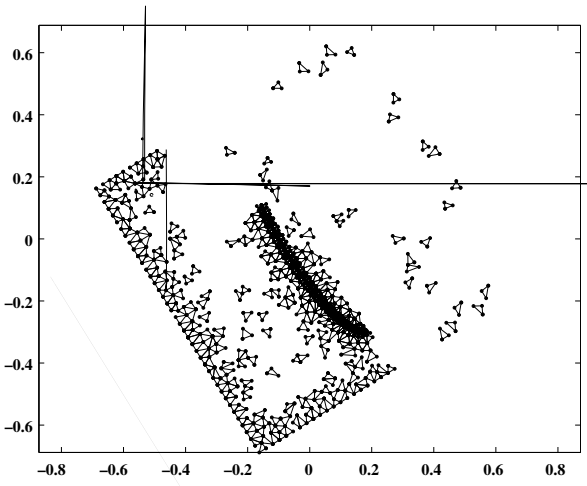

direction of the vertical (compressional) axis. However, in Fig. 6b we show that in our simulations there is no significant difference between these two distances as defined in [7,12]. It is possible that small differences found in the previous studies are due to the way the boundary conditions are imposed. In Hwang's simulations the sides of the unit cell are parallel to the flow axes and the cell length in the vertical direction becomes much smaller than the length in the horizontal direction as the strain increases. D'Avino et al. do not use a periodic cell, instead particles leaving the simulation along the sides of the flow domain are reintroduced at random points along the top boundary. In contrast, our simulations are on a truly periodic lattice in which the orientation of the lattice is not parallel to axes the extensional flow and is periodically replicated so that the unit cell aspect ratio remains close to unity.

7.2. Dynamics and rheology of elliptical particles

7.2.1. One elliptical particle per cell

Circular particles do not rotate on average in a purely extensional flow, since the imposed vorticity is zero. However, an anisotropic particle, see Fig. 8, will rotate to align its major axis with the extensional direction. This is illustrated in Fig. 9[1] for an ellipse of aspect ratio 4.

For the case of an isolated elliptical particle, the angular velocity in planar extensional flow has been obtained analytically by Bilby and Kolbuszewski [2] from the general theory for the motion of ellipsoidal particles in linear flows given by Jeffery [15]. For an ellipse of aspect ratio, r, the angle Θ between the major axis of the ellipse and the extensional direction satisfies,

$$\frac{\mathrm{d}\Theta}{\mathrm{d}\epsilon} = -\frac{r^2-1}{r^2+1}\sin(2\Theta), \tag{31}$$

where ϵ is the strain ($\epsilon = \dot{\epsilon}t$). This provides an analytic solution for the orientation after a strain ϵ of particle initially at angle Θ_0, given by

$$\Theta = \tan^{-1}\left[\mathrm{e}^{-2\epsilon\frac{r^2-1}{r^2+1}}\tan\Theta_0\right]. \tag{32}$$

In a suspension the orientation of a particle is affected by hydrodynamic interactions with neighbouring particles. For a single circular particle in the Kraynik–Reinelt lattice this produces a periodic variation in the orientation of the particle centred around its initial orientation. For elliptical particles this periodic variation is superimposed on the alignment predicted by Eq. (32). In Fig. 10a we plot the evolution of the angle of

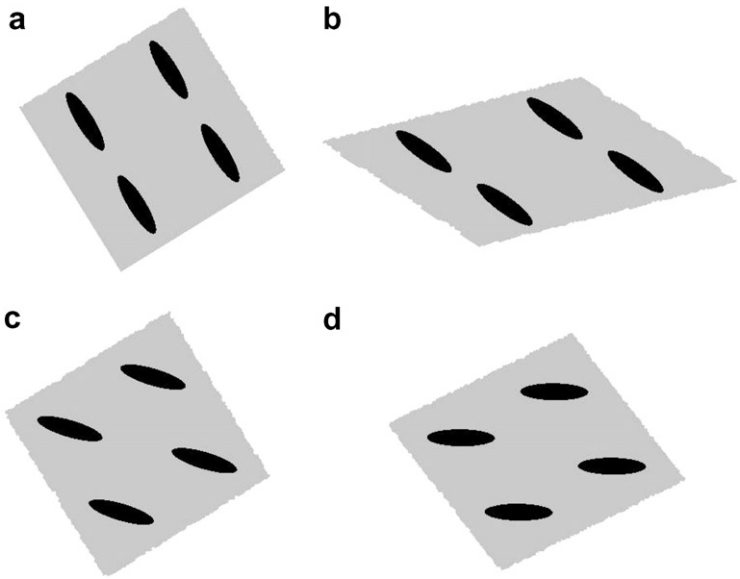

Fig. 9. The motion of a single elliptical particle displayed together with 3 of its images under planar extensional flow at (a) $\epsilon = 0$; (b) $\epsilon = 0.45$ (approximately half the lattice period); (c) $\epsilon = 0.96$ (approximately one lattice period); (d) $\epsilon = 3$. The particle rotate from its initial orientation at angle $\Theta_0 = 2.124$ (=121.7°) to alignment with the extensional axis ($\Theta = \pi$).

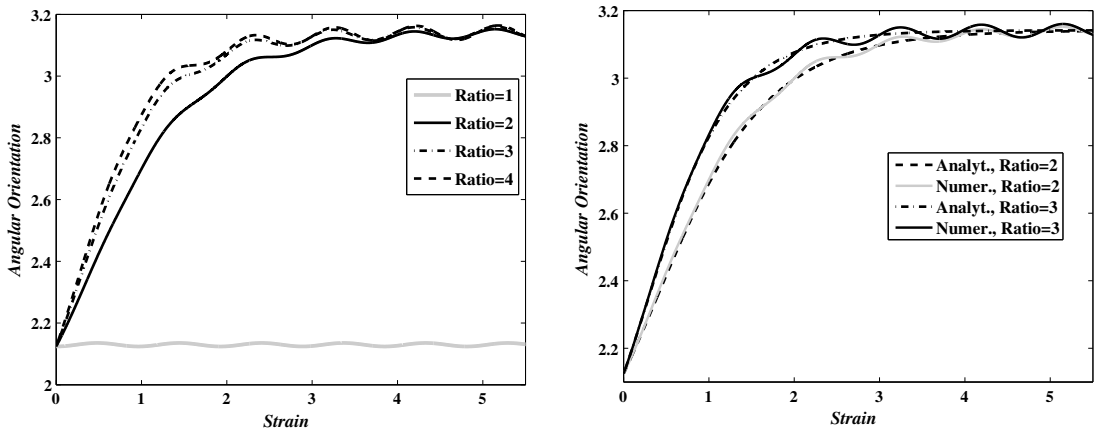

Fig. 10. (a) Plot of the evolution of the orientation angle, Θ of elliptical particles with $\Phi = 0.0942$ initially aligned at $\Theta_0 = 2.124$ for aspect ratios from 1 to 4. (b) Comparison between the numerical results for $\Phi = 0.0942$ and analytical results for $\Phi \to 0$ for aspect ratios 2 and 3.

orientation from an initial angle of $\Theta_0 = 2.124$ for ellipses of aspect ratios 1–4 at an area fraction of $\Phi = 0.0942$. The orientation angle of the circular particle oscillates about its initial orientation, whereas the elliptical particles rotate towards $\Theta_0 = \pi$. In Fig. 10b the evolution of Θ for the ellipses of aspect ratios 2 and 3 are compared to analytical solution in the dilute limit. (The aspect ratio 4 result is left off for clarity.) It can be seen that the only effect of finite area fraction is to introduce a periodic variation on the behaviour predicted by the analytical solution.

The effect of particle rotation is also seen in the transient extensional viscosity, which is shown in Fig. 11a. However, once the particle has become aligned with the extensional axis we can calculate an average extensional viscosity over a lattice period as for circular particles. This is shown in Fig. 11b for an area fraction

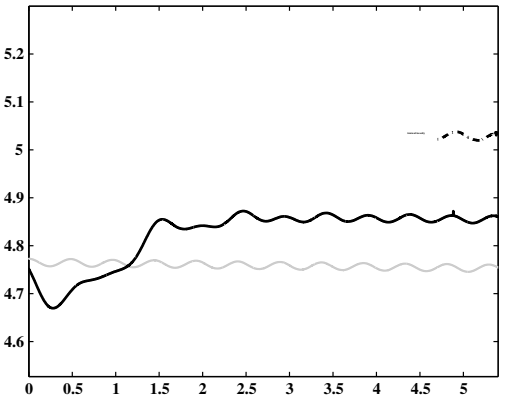

of $\Phi = 0.0942$. For a fixed area fraction the steady state viscosity increases approximately linearly with the aspect ratio. This is consistent with the result that the extensional viscosity is determined by the largest linear dimension of the particle, so that at low area fractions in two dimensions it is proportional to Φ_r.

7.3. Multiple elliptical particles per cell

The previous calculations contain a single particle per unit cell, so that all particles have the same orientation and the interparticle spacing is set by the lattice. The effect of hydrodynamic interactions is to produce a periodic disturbance in orientation about the extensional direction. However, this periodicity is merely an artifact of the constraint imposed by the lattice structure and the real effect of hydrodynamic interactions is to disperse the particle orientations about the extensional axis [20].

In order to relax these restrictions we again place several particles within the unit cell. In Fig. 12[2] we show the evolution of a system containing seven identical elliptical particles of aspect ratio four per unit cell with an area fraction of particles $\Phi = 0.1237$. The calculation was performed using a mesh with 4172 elements. Initially the particles are all aligned at $\Theta_0 = 2.124$, but the orientations become dispersed due to hydrodynamic interactions. In Fig. 13 we compare the average orientation angle and variance about the mean (defined as $\frac{1}{N}\sum(\Theta - \langle\Theta\rangle)^2$) for particles of aspect ratio 4 at $\Phi = 0.0942$ for simulations with 1,7, 14 and 28 particles in order to determine the effects of system size on these statistics. Initially the evolution of the average orientation angle is close to that predicted for a dilute suspension using Eq. (32) however, after a strain of two there are substantial random fluctuations due to interactions between the particles. This is reflected in the variance, which increases for strains up to two and then becomes rather noisy. The average level of the variance does not change with the size of the system, nor is there evidence of long term aggregation.

The average extensional viscosity of the suspension is plotted in Fig. 14. There is an initial transient phase similar to that seen in Fig. 11a while the particles rotate towards alignment with the extensional axis, after which there are fluctuations about an average value due to interactions between the particles. Note however that although the average value for all three multiparticle simulations are approximately the same this value is larger by about 5% than the value found in the single particle simulations. As with the case of circular particles, shown in Fig. 6a, constraining the particles to be equally spaced on the lattice artificially reduces the effect of hydrodynamic interactions. However, it appears that simulations with small numbers of particles (10 or so) produce similar results to those with much larger numbers of particles. In principle there is no limit to the number of particles that can be placed in the unit cell. The only limitation is the need to resolve accu-

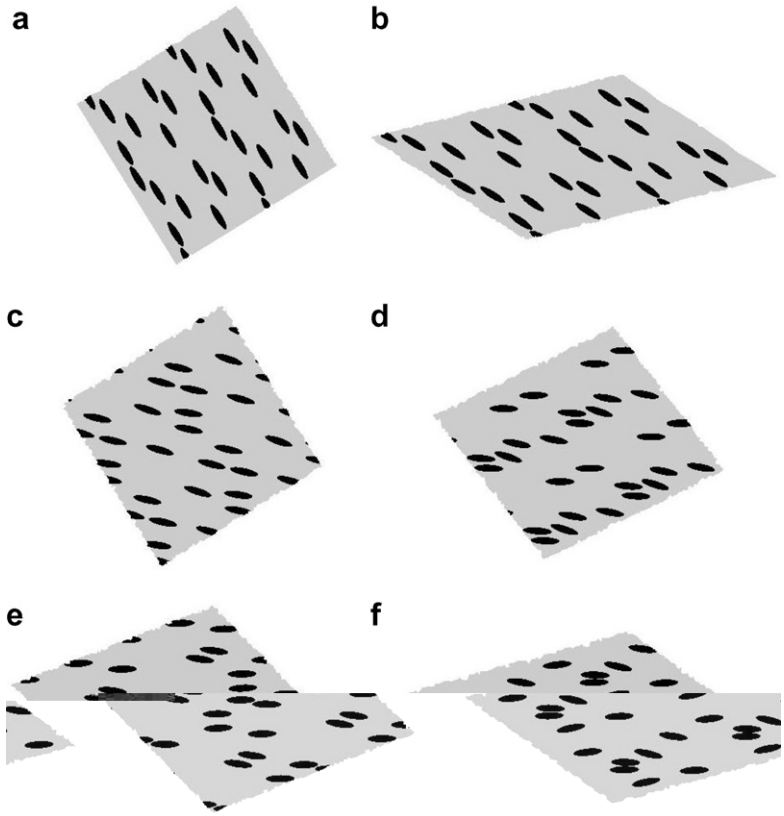

Fig. 12. The motion of seven elliptical particles in a unit cell displayed together with 3 images of the unit cell (a) $\epsilon = 0$; (b) $\epsilon = 0.45$ (approximately half the lattice period); (c) $\epsilon = 0.96$ (approximately one lattice period); (d) $\epsilon = 3$; (e) $\epsilon = 6$; (f) $\epsilon = 12$. The particles rotate towards alignment with the extensional axis but are dispersed due to hydrodynamic interactions.

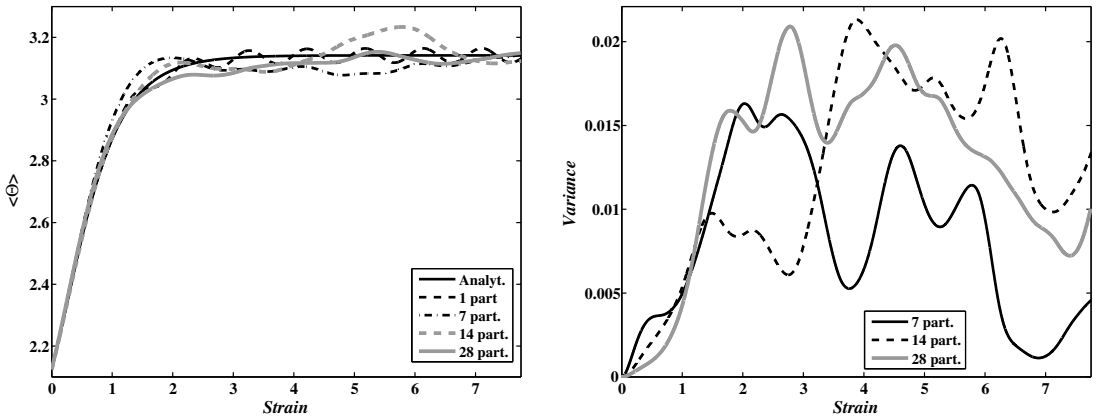

Fig. 13. Comparison of the average particle orientation for simulations with 1, 7, 14 and 28 elliptical particles of aspect ratio 4 at an area fraction of $\Phi = 0.0942$ compared to the analytical solution for $\Phi \to 0$; (b) the variance about this mean angle in the multiparticle simulations.

rately the region between the particles, where there are large lubrication forces keeping the particles apart since we have not introduced an artificial repulsive forces between particles.

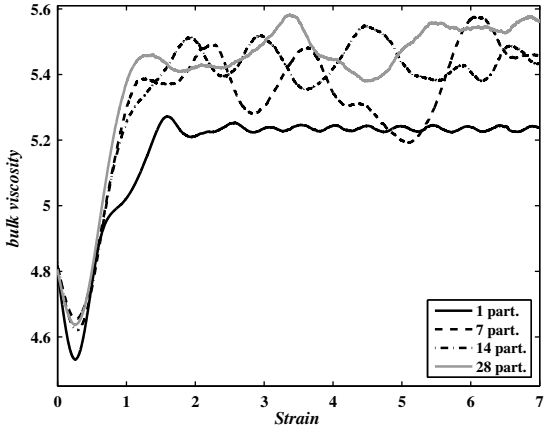

Fig. 14. The extensional viscosity as function of strain for the simulations of Fig. 13.

8. Conclusion

In this paper we describe a novel direct numerical simulation technique for particle suspensions under planar extension flow using a biperiodic self-replicating lattice. This provides a simulation in a truly periodically replicable cell that can be run for arbitrarily large strains. The quotient map representation combined with the Lagrangian finite element method provides a natural way to implement the Kraynik–Reinelt lattice in a manner that is free of any special treatment of cell boundaries. The method can be applied to particles of any shape or mixture of shapes.

The simulation results are found to be in good agreement with analytical solutions for the dilute limit. For circular particles we recover the $\eta = 4\mu(1 + 2\Phi)$ extensional viscosity in the limit $\Phi \to 0$. This approximation remains accurate up to $\Phi \approx 0.1$, but at higher area fractions hydrodynamic interactions produce a nonlinear increase in viscosity. For anisotropic particles the fibres rotate towards alignment with the extensional axis, but with a dispersed orientation distribution due to hydrodynamic interactions.

Although in this paper we have confined our attention to Newtonian fluids we have also applied our method to suspensions in viscoelastic fluids. In viscoelastic fluids our method has the further advantage of enabling the constitutive equation to be solved in the co-deforming frame of the fluid [10]. This enables the constitutive equation to be solved as ordinary differential equations along characteristics. Furthermore, by replacing the traction force around the particles with a finite element solution for the interior we can analyse suspensions of deformable particles and emulsions.

The simulations in this paper are for a two-dimensional fluid where the particles are effectively infinitely long cylinders. For planar extensional flow this method could be extended to three-dimensional suspensions by replacing triangular elements with tetrahedral elements. Recently Morrison and Rallison [18] have extended the Lagrangian method of [10] to fully three-dimensional time-dependent viscoelastic flows and have successfully simulated viscoelastic flow around a sedimenting sphere. However, for Newtonian fluids the additional complexity of reconnecting a three-dimensional compared to a two-dimensional grid makes the fully Lagrangian scheme computationally expensive compared to other methods such as Arbitrary Lagrangian–Eulerian (ALE) schemes that produce less mesh distortion. Though for viscoelastic fluids with complex constitutive models this may be outweighed by simplification of the stress calculation for Lagrangian methods. Another restriction is that our method relies on the existence of a periodically self-replicating lattice and so cannot be used for uniaxial extension for which no such lattice exists.

Acknowledgments

We are grateful to the EPSRC for financial support through the Microscale Polymer Processing project GR/T11807/01. We would also like to thank Jonathan Shewchuk for the "Triangle" grid generation program and Tim Nicholson for the "FlowDis" visualisation software.

Appendix A. Supplementary data

Supplementary data associated with this article can be found, in the online version, at doi:10.1016/j.jcp.2008.04.035.

References

[1] G.K. Batchelor, The stress system in a suspension of force-free particles, J. Fluid Mech. 41 (1970) 545.
[2] B.A. Bilby, M.L. Kolbuszewski, The finite deformation of an inhomogeneity in two-dimensional slow viscous incompressible flow, Proc. Roy. Soc. Lond. A 355 (1977) 335.
[3] E.S. Boek, P.V. Coveney, H.N.W. Lekkerkerker, P. van der Schoot, Simulating the rheology of dense colloidal suspensions using dissipative particle dynamics, Phys. Rev. E 55 (1997) 33124.
[4] J.F. Brady, G. Bossis, Stokesian dynamics, Annu. Rev. Fluid Mech. 20 (1988) 111.
[5] J.F. Brady, The Einstein viscosity correction in a *n* dimensions, Int. J. Multiphase Flow 10 (1984) 113.
[6] S. Chen, G.D. Doolen, Lattice Boltzmann method for fluid flows, Annu. Rev. Fluid Mech. 30 (1998) 329.
[7] G. D'Avino, P.L. Maffettone, M.A. Hulsen, G.M.W. Peters, A numerical method for simulating concentrated rigid particle suspensions in an elongational flow using a fixed grid, J. Comput. Phys. (2007), doi:10.1016/j.jcp.2007.04.027.
[8] B.N. Delaunay, Sur la sphere vide, Bull. Acad. Sci. USSR VII: Class. Sci. Math. 793 (1934).
[9] R. Glowinski, T.-W. Pan, T.I. Hesla, D. Joseph, A distributed Lagrange multiplier/fictitious domain method for particulate flows, Int. J. Multiphase Flow 25 (1999) 755.
[10] O.G. Harlen, J.M. Rallison, P. Szabo, A split Lagrangian–Eulerian method for simulating transient viscoelastic flows, J. Non-Newtonian Fluid Mech. 60 (1995) 81.
[11] D.M. Heyes, Molecular dynamics simulations of extensional sheet and unidirectional flow, Chem. Phys. 98 (1985) 15.
[12] W.R. Hwang, M.A. Hulsen, Direct numerical simulations of hard particle suspensions in planar elongational flow, J. Non-Newtonian Fluid Mech. 136 (2006) 67.
[13] W.R. Hwang, M.A. Hulsen, H.E.H. Meijer, Direct simulation of particle suspensions in sliding bi-periodic frames, J. Comput. Phys. 194 (2004) 742.
[14] H.H. Hu, Direct simulation of flows of solid–liquid mixtures, Int. J. Multiphase Flow 22 (1996) 335.
[15] G.B. Jeffery, The motion of ellipsoidal particles immersed in a viscous fluid, Proc. Roy. Soc. Lond. A 102 (1922) 61.
[16] A.M. Kraynik, D.A. Reinelt, Extensional motions of spatially periodic lattices, Int. J. Multiphase Flow 18 (1992) 1045.
[17] A.W. Lees, S.F. Edwards, The computer study of transport processes under extreme conditions, J. Phys. C 5 (1972) 1921.
[18] N.F. Morrison, J.M. Rallison, Transient 3D flow of polymer solutions, in: Presented at XVth International Workshop on Numerical Methods for Non-Newtonian Flows, Rhodes, 2007.
[19] C.J.S. Petrie, One hundred years of extensional flow, J. Non-Newtonian Fluid Mech. 137 (2006) 1.
[20] E.S.G. Shaqfeh, D.L. Koch, Orientational dispersion of fibers in extensional flows, Phys. Fluids A 2 (1990) 1077.
[21] J.R. Shewchuk, Triangle: engineering a 2D quality mesh generator and Delaunay triangulator, Lect. Notes Comput. Sci. 1148 (1996) 203.
[22] R. Sibson, Locally equiangular triangulation, Comput. J. 21 (1977) 243.
[23] D. Silvester, A. Wathen, Fast iterative solution of stabilised Stokes systems. Part 2: using general block preconditioners, SIAM J. Numer. Anal. 30 (1994) 630.